



Direct observations of thermalization to a Rayleigh–Jeans distribution in multimode optical fibres

Hamed Pourbeyram^{1,4}, Pavel Sidorenko^{1,4}, Fan O. Wu^{1b,2,4}, Nicholas Bender¹, Logan Wright^{1b,3}, Demetrios N. Christodoulides^{1b,2} and Frank Wise^{1b,✉}

Nonlinear multimode optical systems support a host of intriguing effects that are impossible in single-mode settings. Although nonlinearity can provide a rich environment where the chaotic power exchange among thousands of modes can lead to novel behaviours, understanding and harnessing these processes to our advantage is challenging. Over the years, statistical models have been developed to macroscopically describe the response of these complex systems. One of the cornerstones of these theoretical formalisms is the prediction of a photon–photon-mediated thermalization process that leads to a Rayleigh–Jeans distribution of mode occupations. Here we report the use of mode-resolved measurement techniques to directly observe the thermalization to a Rayleigh–Jeans power distribution in a multimode optical fibre. We experimentally demonstrate that the underlying system Hamiltonian remains invariant during propagation, whereas power equipartition takes place among degenerate groups of modes—all in full accordance with theoretical predictions. Our results may pave the way towards a new generation of high-power optical sources whose brightness and modal content can be controlled using principles from thermodynamics and statistical mechanics.

Nonlinear interactions in many-mode systems are ubiquitous in nature. In condensed-matter physics, for example, anharmonic processes are known to limit the thermal conductivity of solids and are behind high-temperature superconductivity in binary alloy systems^{1,2}. The role of nonlinearity in lattices with many degrees of freedom was first explored in the 1950s by Fermi et al.³ in an effort to support the ergodic hypothesis during thermalization—a seminal study that ushered in the development of soliton and ergodic theories, chaos and integrable systems⁴. Appreciation of the profound effects that nonlinearities can have on fields that propagate in multimode structures such as cavities, waveguides and random media^{5,6} has driven renewed interest in addressing these issues in optical settings. The resurgence of interest in systems that support a multitude of modes is driven by the promise of high-bandwidth communication networks⁷ and high-power light sources⁸. Along these lines, a series of experiments have been carried out in multimode silica fibres where a number of surprising effects have been observed^{9–16}, such as geometric parametric instabilities^{11,12,17}, broadband supercontinuum^{17,18} and new families of spatiotemporal dispersive waves^{9,16}. In addition, a somewhat unexpected effect has been independently reported in several studies, where, at high intensities, power is found to redistribute itself in a manner that favours the lower groups of spatial eigenmodes of the fibre—the so-called beam self-cleaning effect¹⁰. This peculiar process has nothing to do with self-focusing or Raman effects; energy is exchanged among the modes by four-wave mixing. In view of these developments, a new set of theoretical challenges arose in terms of interpreting and predicting the complex nonlinear response of such systems, especially when a large number of modes are involved. This complexity can be readily appreciated by keeping in mind that in a

nonlinear system that supports M modes, one must account for M^2 cross-phase modulation products and M^4 four-wave mixing pathways through which the modes can exchange energy¹⁹. The analysis of this class of problems is exceedingly complex, and it is difficult to glean physical insights from computational approaches.

To address these issues, models have been put forward based on notions from wave turbulence/kinetic theories^{20–24} and statistical mechanics^{25–28}. A central prediction of these theories is that the power in nonlinear multimode systems should irreversibly settle after thermalization (that is, in thermal equilibrium) into a Rayleigh–Jeans (RJ) distribution^{20,21,26,27}, which is uniquely characterized by optical temperature T and chemical potential μ . In general, once the RJ distribution is reached, power $|c_i|^2$ that occupies mode i is given by $|c_i|^2 = -T/(\beta_i + \mu)$, where β_i is the linear propagation constant (eigenvalue) associated with the mode. We note that the RJ distribution in such multimode arrangements is all-optically induced via multi-wave mixing (Fig. 1a) as the system maximizes its entropy in phase space. The sole function of nonlinearity is to chaotically reallocate power among the modes so that ergodicity is thermodynamically manifested. During propagation, the system is constrained to move on constant-power ($P = \sum_i |c_i|^2$) and Hamiltonian ($H = \sum_i \beta_i |c_i|^2$) isosurfaces. In high-quality fibres, power is preserved during propagation, whereas the linear Hamiltonian is also a constant of motion since it physically represents the longitudinal momentum flow of the electrodynamic field²⁶, as expected from the zz component of the electromagnetic stress tensor, T_{zz} (ref. 29). In all these cases, the optical temperature and chemical potential represent thermodynamic forces that govern the flow of longitudinal momentum and power, respectively,

¹School of Applied and Engineering Physics, Cornell University, Ithaca, NY, USA. ²CREOL/College of Optics and Photonics, University of Central Florida, Orlando, FL, USA. ³Physics & Informatics Laboratories, NTT Research, Sunnyvale, CA, USA. ⁴These authors contributed equally: Hamed Pourbeyram, Pavel Sidorenko, Fan O. Wu. ✉e-mail: frank.wise@cornell.edu

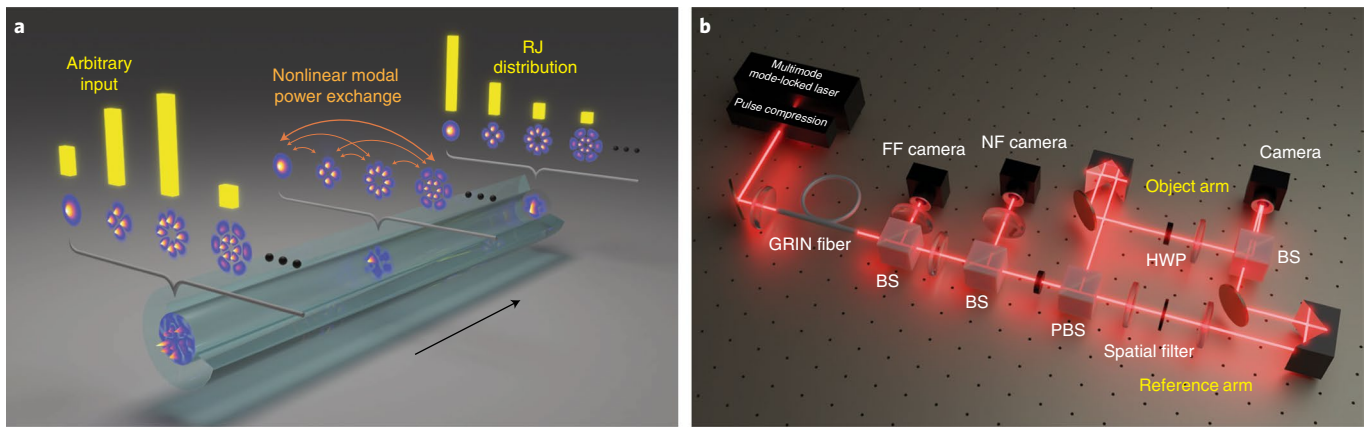


Fig. 1 | Process of optical thermalization and experimental setup used to observe RJ distribution. **a**, Schematic depicting the evolution to optical thermal equilibrium in a nonlinear multimode fibre, arising from four-wave mixing interactions among a multitude of optical guided modes. A superposition of these modes launched into the multimode fibre eventually settles into an RJ distribution, thus signifying the onset of thermal equilibrium. **b**, Experimental arrangement used to demonstrate optical thermalization to an RJ distribution. A multimode mode-locked laser generates femtosecond-duration pulses that consist of multiple transverse modes locked together. The pulses exit the laser with large frequency chirp, which is removed in the compressor to launch pulses with peak powers up to 70 kW in the multimode GRIN fibre. For experiments with speckle-pattern inputs, a spatial light modulator is inserted between the laser and multimode fibre. The near- and far-field profiles of the output beam are then recorded, and the beam is sent to the interferometric off-axis digital holography setup for spatiotemporal characterization. BS, beamsplitter; NF, near field; FF, far field; PBS, polarizing beamsplitter; HWP, half-wave plate.

in a closed Hamiltonian system³⁰. The wave turbulence description of wave condensation—a process found to be related to beam self-cleaning—requires the introduction of a frequency cutoff to avoid divergence of energy for condensation: another study³¹ pointed out that a parabolic-index waveguide provides such a cutoff. In the last two years, experimental efforts have exposed some of the ramifications of the expected RJ distribution in multimode optical fibres¹⁴. From the near-field and far-field intensity profiles measured in beam-cleaning experiments, the average occupancy of the fundamental mode was determined³² during condensation. The corresponding entropy and heat capacity were consistent with equilibrium thermodynamics. In addition, it was shown that the average mode number is conserved in this process¹⁵. Although the measurement of the fundamental mode occupancy agrees with the theoretical prediction on average, the distribution cannot be inferred by only monitoring the fundamental mode.

In this paper, we provide unequivocal demonstration of RJ thermalization in a multimode optical fibre. Modal decomposition of the directly measured spatial profile of the complex electric field³³ reveals how the modal groups are populated throughout the thermalization process. For some initial conditions, the thermal distribution can be reached after a few characteristic nonlinear lengths of propagation. We find that power equipartition takes place among degenerate groups of modes, in accordance with theoretical expectations. We find that the output beam quality is invariant, even after the onset of beam self-cleaning.

The experimental arrangement used to observe the thermalization processes is illustrated in Fig. 1b. A fibre laser⁸ generates 200 fs pulses at 1,040 nm that consist of multiple transverse modes locked together in time. With pulse energy of about 20 nJ, the peak power can be as high as 70 kW. The pulses are launched into various lengths of graded-index (GRIN) multimode fibre. Unless specified otherwise, the fibre has a 50 μm core diameter, numerical aperture (NA) of 0.2 and zero-dispersion wavelength near 1,300 nm. The GRIN fibre is chosen because its equally spaced propagation constants facilitate multi-wave mixing (in this case, four-wave mixing) interactions among the modes (Supplementary Fig. 1). This fibre supports about 220 spatial eigenmodes (110 in each polarization) at 1,040 nm. Different combinations of transverse modes can be

excited by controlling the position and angle of the lens that couples light into the fibre and maintaining 80% coupling efficiency, and the losses are negligible. Although the input field is linearly polarized, the polarization changes as the pulse accumulates the nonlinear phase. The output is projected onto a basis of orthogonal linear polarizations (Methods). For each polarization, the complex electric field is measured by off-axis digital holography and decomposed into a spectrally resolved eigenmode basis (Methods and Supplementary Section 2). The modal power $|c_k|^2$ is obtained by summing the contributions of the two polarizations. The peak power is used as a control parameter to observe the evolution to a thermal distribution. Each measured modal distribution is an average over $\sim 10^{10}$ pulses, which exhibit $\sim 1\%$ fluctuations in peak power. Short lengths of fibre were chosen for the experiments to preclude the possibility of stimulated Raman scattering. With fibre lengths between 0.5 and 2.5 m and bending radii of about 0.4 m, linear mode coupling is weak. The differential group delay between the modes in the used parabolic GRIN fibre is small compared with the effects of chromatic dispersion. The characteristic (chromatic) dispersion length is $L_{\text{DS}} \approx 0.5$ m, whereas the nonlinear length is $L_{\text{NL}} \approx 5$ cm for the highest-energy pulses launched into the fibre (the characteristic lengths are defined in Supplementary Section 7).

When the launched beam has some overlap with the fundamental mode of the fibre, the process of thermalization can be observed. Typical results obtained in a 50-cm-long segment of the fibre, with a 50 μm core diameter, will be described first. The beam profiles and modal decompositions observed at the output of the fibre are shown in Fig. 2 for the indicated range of input peak powers. The total power conveyed in each mode group is averaged over its degeneracy g_k to plot the mode occupancy versus propagation constant. Because the linear mode coupling is weak, the distribution (Fig. 2, top) reflects the modal composition of the launched field. As the peak power is increased above ~ 10 kW, the spatial profile becomes an intense bell-shaped lobe with approximately the diameter of the fundamental mode of the fibre, accompanied by a low-intensity background. As the power increases, the measured modal occupancies clearly evolve from the initial non-equilibrium distribution at the input to a thermal-equilibrium state. The modal decomposition is performed for each frequency in the spectrum, where it is

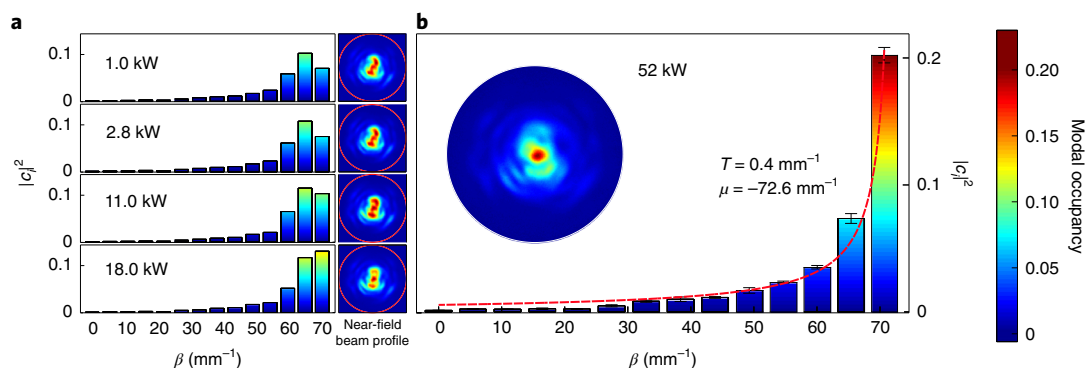


Fig. 2 | Experimental observation of optical thermalization to an RJ distribution. **a**, Output power distributions among the mode groups of the GRIN fibre and their corresponding output near-field intensity profiles, as the total input power increases. The circles in the insets are the core-cladding boundary. The modes are interrogated using interferometric off-axis digital holography. The distributions are plotted against the differential propagation constant; for the k th mode group, this is defined as $\beta_k = \beta_k - k_0 n_{\text{cladding}}$ where β_k denotes the actual propagation constant, $k_0 = 2\pi/\lambda_0$, λ_0 is the vacuum wavelength, and n_{cladding} is the index of refraction of the cladding. The distribution at 1 kW (the lowest power level) represents the relative power levels initially launched in the various mode groups at the input. As the power increases, the modal occupancies $|c_k|^2$ are nonlinearly reshuffled. **b**, Direct observation of an RJ distribution on optical thermalization, which occurs at 52 kW. The thermal-equilibrium RJ state observed in the experiment is characterized by temperature $T = 0.42 \text{ mm}^{-1}$ and chemical potential $\mu = -73.00 \text{ mm}^{-1}$. The error bars represent the uncertainties (Supplementary Section 5). The dashed curve ($T = 0.4 \text{ mm}^{-1}$ and $\mu = -72.6 \text{ mm}^{-1}$) depicts the RJ distribution theoretically expected from the excitation conditions. The discrepancy from the measured distribution for higher-order modes is attributed to the deviation from an ideal parabolic-index profile (Supplementary Section 6). Here the beam self-cleaning effect in the near field is also apparent (inset). In all the cases, the distributions are plotted in a normalized fashion ($\sum_k g_k |c_k|^2 = 1$), where $g_k = k$ represents the mode-group degeneracy, whereas the twofold polarization degeneracy has been implicitly accounted for here. These experiments were conducted in 0.5 m GRIN fibre with a 50 μm diameter core.

appreciable. At a peak power of 52 kW, an RJ distribution is observed. From the initial modal distribution (recorded at an input power of 1 kW), one can directly predict the optical temperature and chemical potential by invoking the universal equation of state, namely, $H + \mu P = -MT$, where M represents the number of participating modes and $P = \sum_k |c_k|^2$ is the total power flowing in the system²⁶ (Supplementary Section 9). Here, for convenience, the total power flowing in the system is now normalized to unity. Under these conditions, as well as from the input excitation data, theory predicts that this system should settle to an RJ distribution with $T = 0.4 \text{ mm}^{-1}$ and $\mu = -72.6 \text{ mm}^{-1}$ (Fig. 2b, dashed curve). Experiments carried out at this power level reveal that the system indeed relaxes to an RJ distribution with $T = 0.42 \text{ mm}^{-1}$ and $\mu = -73.00 \text{ mm}^{-1}$, in close agreement with theory. We emphasize that the theoretical curve in Fig. 2b is determined from the initial distribution (that is, $T = 0.40 \text{ mm}^{-1}$) and is not a fit to the final distribution (which would yield $T = 0.42 \text{ mm}^{-1}$). The mode-resolved technique employed in our experiment provides irrefutable evidence of the RJ distribution that was theorized in earlier works^{20,21,26–28}.

Although the result shown in Fig. 2 is associated with the single-input condition, the convergence to an RJ distribution is a more general phenomenon. To demonstrate this, we illuminated a 2.5-m-long parabolic-index fibre (62.5 μm core diameter and NA of 0.275, supporting 812 modes in both polarizations) with an ensemble of statistically equivalent random input states (speckled fields) and determined the modal-occupancy probability density function (PDF) of the entire ensemble at the output, for different input pulse powers (Methods and Supplementary Section 10). In Fig. 3a, we show that for a sufficiently high peak power ($\sim 20 \text{ kW}$), the ensemble-average modal-occupancy PDF converges to an RJ distribution, which can be predicted from the ensemble-average PDF of a set of low-power ($\sim 2 \text{ kW}$) pulses. This means that for any equivalent random-input condition, the corresponding output modal-occupancy distribution statistically converges to an RJ distribution for appropriate input powers. An example low-power output pattern is shown in Fig. 3b for reference. From the ensemble

of low-power pulses, we find $H = \sum_i \beta_i \langle |c_i|^2 \rangle \cong 128.0 \text{ mm}^{-1}$, which

allows us to predict the equilibrium temperature and chemical potential ($T = 0.3 \text{ mm}^{-1}$ and $\mu = -178.0 \text{ mm}^{-1}$) of the ensuing RJ distribution (Fig. 3e, red line) that corresponds to the high-power ensemble. Figure 3c–f displays the measurements of different 20 kW wavelength-resolved output intensity patterns, each generated by a different speckled input. The spatial concentration of the intensity at the centre of the fibre core in Fig. 3c–f, relative to Fig. 3b, reflects the speckle ensemble's convergence to an RJ distribution.

It is worth noting that the experiment shown in Fig. 2 was performed under conditions corresponding to a microcanonical ensemble: a single-input field pattern was used, where both power and Hamiltonian of the system were invariant during the evolution. On the other hand, the experiment shown in Fig. 3 is effectively performed under canonical-like conditions^{30,34}, because the ensembles of speckle patterns were used. Each speckle pattern is uncorrelated with the other elements in the ensemble, and its precise properties fluctuate relative to the ensemble average. The speckle patterns fluctuate but yield, on average, a modal power distribution, whereas the value of the Hamiltonian fluctuates in a similar manner with a constant expectation value. This is formally equivalent to a standard canonical-like thermodynamic setting, where the system is allowed to exchange energy with a heat bath in a statistical manner, whereas—on average—its internal energy is constant^{30,34}. In this case, the ensemble-average quantities can be used to predict optical thermodynamic behaviours. As shown in Fig. 3, the experimental results are in good agreement with theory, which demonstrates the true thermodynamic nature of the process.

Once a modal distribution reaches RJ equilibrium, the distribution values should not change with further evolution. Experiments were performed with longer fibres and/or higher peak powers to verify that the process is indeed irreversible. In these experiments, the beam from the mode-locked laser was used to excite the fibre with a 50 μm core (Fig. 2). By increasing the input power, the nonlinear length L_{NL} can be adjusted. For peak powers as high as 70 kW

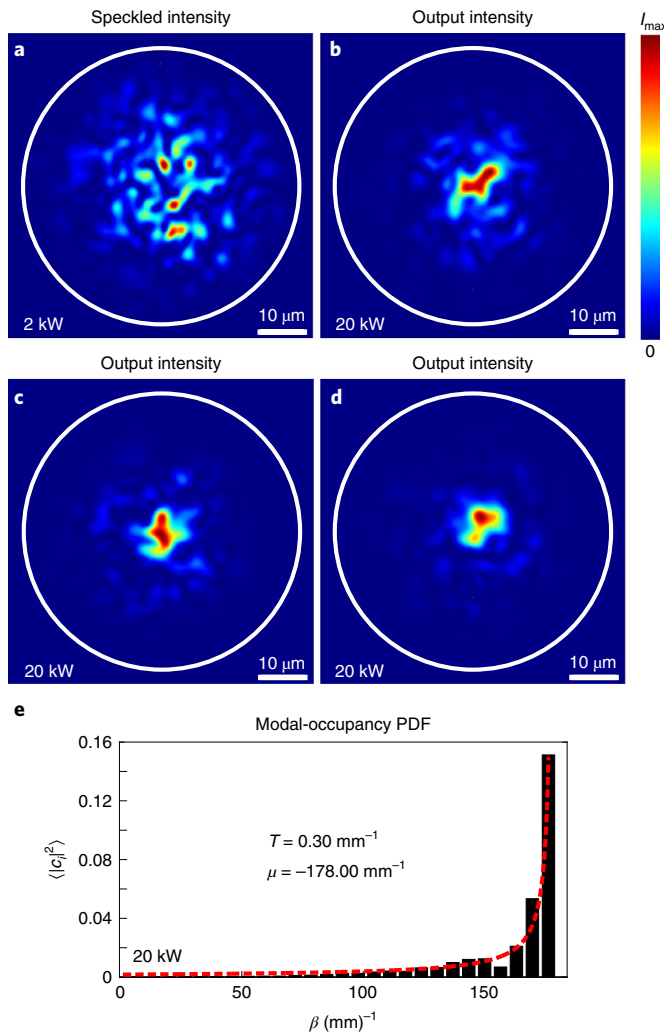


Fig. 3 | RJ ensemble produced by speckled input fields. **a**, Typical low-power speckle pattern observed at the output of 2.5 m GRIN fibre with 62.5 μm core diameter. **b–d**, Example intensity profiles observed at the output of the fibre with a peak input power of 20 kW. Beam self-cleaning is evident in the profiles. **e**, Observed RJ distribution after averaging over an ensemble of input speckle patterns (similar to the pattern in **a**) at 20 kW. The ensemble-average output modal-occupancy PDF, generated by 14 independent speckled input pulses, is represented by the black bars. The red dashed line is the theoretical RJ distribution obtained from the initial conditions. These results were obtained at a wavelength of 1,030 nm.

launched into a 1.5 m fibre, $L \approx 30L_{\text{NL}}$. With these parameters, the spectrum begins to show some asymmetry from stimulated Raman scattering (Supplementary Fig. 10). As shown in the experiments described in Fig. 2, the occupation of the fundamental (LP_{01}) mode reaches and retains its equilibrium value after propagating a few nonlinear lengths (Fig. 4a). The normalized mean-square error (NMSE) between the measured and expected RJ distributions decreases in the first few nonlinear lengths and remains approximately constant beyond that point (Fig. 4b). Another signature of RJ thermalization in the microcanonical ensemble is the equipartition of power among the modes within the same mode group: $|c_i|^2 = -T/(\beta_i + \mu)$; therefore, modes with the same propagation constant β_i should be equally populated at thermal equilibrium. Plots of the occupancies of modes in each group are displayed in Supplementary Figs. 15 and 16. We quantify the variation in mode occupancies by calculating the mean coefficient of variation (CV) for the first six mode groups,

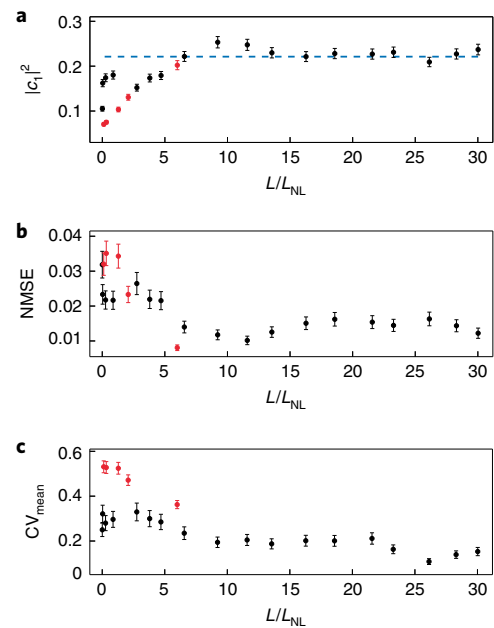


Fig. 4 | Irreversibility of optical thermalization. The figures provide information about various signatures of optical thermalization in a nonlinear multimode GRIN fibre, before and after the system attains an RJ distribution. In our experiments, the fibre length L is fixed, and the unfolding of thermalization is monitored as a function of L/L_{NL} , where nonlinear length L_{NL} decreases with increasing input power. The red and black symbols represent measurements obtained in a 0.5-m- and 1.5-m-long fibre, respectively. The error bars represent uncertainties (Supplementary Section 5). **a**, Power residing in the fundamental (LP_{01}) mode. The dashed blue line denotes the power occupancy of the fundamental mode, as expected from theory, once the RJ distribution is established. Although in the short (0.5 m) fibre, thermal equilibrium is obtained at the highest power level (~52 kW), in the longer (1.5 m) segment, the onset of RJ thermalization is established at ~17 kW and remains at this level thereafter. **b**, NMSE, a measure of the deviation from the theoretical anticipated RJ distribution, as a function of L/L_{NL} . As in **a**, the NMSE is irreversibly minimized at the same power levels for the corresponding fibre lengths. **c**, Mean coefficient of variation (CV_{mean}) within the first six mode groups. On thermalization, CV_{mean} is reduced from 0.32 to 0.15 in the 1.5 m fibre; the standard deviation of the modal occupancies among the modes within the same group is suppressed. This signifies equipartition of power within the degenerate modes belonging to the same group, as expected from the RJ distribution. These experiments were conducted in the GRIN fibre with a 50 μm diameter core.

namely, $\text{CV}_{\text{mean}} = \frac{1}{6} \sum_{k=1}^6 \frac{\sigma_k}{\overline{|c_k|^2}}$, where $\overline{|c_k|^2}$ is the mean occupancy of

mode group k and σ_k is the standard deviation in the modal occupancy. In our experiment, the mean CV decreases from 0.32 to 0.15 once thermalization takes place (Fig. 4c). Thus, the powers within the degenerate modes of the same group tend to equalize, in accordance with theory.

Numerical simulations based on coupled nonlinear Schrödinger equations¹⁹ were performed to gain further insights into the thermalization process. Details of these simulations are given in Methods. The measured low-power modal distribution of Fig. 2 was taken as the input field. After an initial exchange of energy between the modes, the occupancy of the fundamental (LP_{01}) mode increases and becomes dominant after about 15 cm of propagation (Fig. 5a). Beyond 20 cm, little energy is exchanged between the modes. The numerical results agree with the measured modal distributions as the power is varied. In particular, the distribution corresponding to

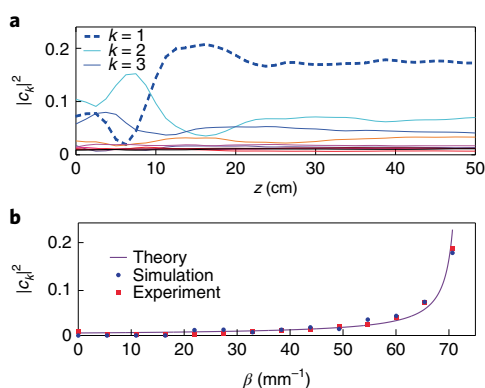


Fig. 5 | Numerical simulations of the optical thermalization process leading to an RJ distribution. **a**, Normalized modal power occupancies per mode $|c_k|^2$ in each degenerate group k as obtained from numerical simulations carried out in a 0.5 m GRIN fibre with 52 kW input power. The simulations involve the first ten mode groups and the resulting coupled nonlinear Schrödinger equations were solved using a massively parallel algorithm. In **a**, the power evolution in the first three mode groups is labelled. **b**, Comparison of the numerical results depicted in **a**, theoretically predicted thermal RJ distribution and experimental results shown in Fig. 2b.

52 kW agrees well with both experimental observations and theoretically predicted RJ equilibrium state (Fig. 5b). Simulations that demonstrate the evolution to RJ distribution for a range of input powers and fibre lengths are shown in Supplementary Fig. 17.

As previously indicated, in the microcanonical ensemble, the invariance of the system's Hamiltonian H during propagation is of paramount importance in establishing the thermodynamic conditions required to observe the RJ distribution^{21,26}. Under quasi-linear conditions, that is, when the intensity is relatively low as in our experiments, one can directly show that the Hamiltonian invariant (H) of the system is dominated by its linear kinetic component (Supplementary Section 20). We verified that the used fibre has negligible losses due to leaky radiation modes and random position-dependent mode-coupling effects. For a given fibre length, as the input peak power is increased, the output spectrum broadens due to self-phase modulation, but remains symmetric and relatively narrowband (the bandwidth is $\sim 3\%$ of the carrier frequency). We measure the Hamiltonian in two different ways: by the direct evaluation of $H = \sum_i^\beta |c_i|^2$ from the mode-resolved measurements of the output beam and by measuring the ratio of the second moments of the near- and far-field beam profiles, which is proportional to the Hamiltonian in the case of a GRIN fibre (Supplementary Section 13). Both measurements were found to remain constant over the range of input powers employed in the experiments (Supplementary Fig. 19). Conservation of the Hamiltonian implies that although the power is reshuffled during thermalization through multi-wave mixing, the total photon momentum per watt is preserved. This is consistent with the redistribution of power in both directions in the mode space, from intermediate to both lower- and higher-order modes¹⁵. Although the output-beam near-field profile (Fig. 2) seems to improve at 52 kW compared with that at 1 kW, the beam quality (M^2 factor³⁵) remains unchanged. This is expected given that M^2 is proportional to the Hamiltonian, which is a constant of motion.

Of course, broad questions remain regarding the observability and universality of thermalization. Fundamentally, the process is universal. However, the equilibrium distribution may not be reached in every experimental setting before dissipation or other competing processes (such as stimulated Raman scattering) occur. The equidistant eigenvalues in the GRIN fibre facilitate phase matching of the four-wave mixing processes that exchange power among the modes

(Supplementary Section 1) and underlie thermalization, and the presence of even weak disorder is known to accelerate the process¹⁴. Processes that weaken nonlinear interactions among the modes naturally hinder thermalization. It is more difficult to phase match four-wave mixing in a step-index fibre than a GRIN fibre. Thus, higher power is required to observe thermalization in step-index fibres (Supplementary Section 21), and stimulated Raman scattering becomes harder to avoid. Multimode hollow-core fibres filled with atomic gases could be useful in thermalization experiments since the Raman process is no longer a limitation. Fibres are only a small subset of multimode optical systems; optical thermodynamics also apply to cavities, multipass cells and integrated optical platforms that support multiple modes.

The direct observation of irreversible thermalization to an RJ distribution in a GRIN fibre is an important step in harnessing thermodynamic concepts in multimode optical dynamics. More importantly, it provides a verification of optical thermodynamic theories that are based on entropic principles. Although the observation of RJ thermalization was carried out in a fibre setting, we expect that these processes will be observed in a variety of environments involving other degrees of freedom such as frequency, optical angular momentum and spin. Finally, it will be interesting to explore some of the other ramifications of optical thermodynamics. These include the observation of equilibria at negative temperatures, isentropic processes, Joule expansions and optical cooling. In addition to unveiling new physics associated with nonlinear complex systems, the thermodynamic approaches could ultimately inspire the design of a new generation of high-performance light sources.

Online content

Any methods, additional references, Nature Research reporting summaries, source data, extended data, supplementary information, acknowledgements, peer review information; details of author contributions and competing interests; and statements of data and code availability are available at <https://doi.org/10.1038/s41567-022-01579-y>.

Received: 1 July 2021; Accepted: 5 March 2022;

Published online: 28 April 2022

References

1. Zhao, L.-D. et al. Ultralow thermal conductivity and high thermoelectric figure of merit in SnSe crystals. *Nature* **508**, 373–377 (2014).
2. Yildirim, T. et al. Giant anharmonicity and nonlinear electron-phonon coupling in MgB_2 : a combined first-principles calculation and neutron scattering study. *Phys. Rev. Lett.* **87**, 037001 (2001).
3. Fermi, E., Pasta, P., Ulam, S. & Tsingou, M. *Studies of the Nonlinear Problems* (Los Alamos Scientific Lab., 1955).
4. Infeld, E. & Rowlands, G. *Nonlinear Waves, Solitons and Chaos* 2nd edn (Cambridge Univ. Press, 2000).
5. Kippenberg, T. J. & Vahala, K. J. Cavity optomechanics: back-action at the mesoscale. *Science* **321**, 1172–1176 (2008).
6. Razzari, L. et al. CMOS-compatible integrated optical hyper-parametric oscillator. *Nat. Photon.* **4**, 41–45 (2010).
7. Richardson, D., Fini, J. & Nelson, L. Space-division multiplexing in optical fibres. *Nat. Photon.* **7**, 354–362 (2013).
8. Wright, L. G., Christodoulides, D. N. & Wise, F. W. Spatiotemporal mode-locking in multimode fiber lasers. *Science* **358**, 94–97 (2017).
9. Wright, L. G., Christodoulides, D. N. & Wise, F. W. Controllable spatiotemporal nonlinear effects in multimode fibres. *Nat. Photon.* **9**, 306–310 (2015).
10. Krupa, K. et al. Spatial beam self-cleaning in multimode fibres. *Nat. Photon.* **11**, 237–241 (2017).
11. Longhi, S. Modulational instability and space time dynamics in nonlinear parabolic-index optical fibers. *Opt. Lett.* **28**, 2363–2365 (2003).
12. Krupa, K. et al. Observation of geometric parametric instability induced by the periodic spatial self-imaging of multimode waves. *Phys. Rev. Lett.* **116**, 183901 (2016).
13. Pourbeyram, H., Agrawal, G. P. & Mafi, A. Stimulated Raman scattering cascade spanning the wavelength range of 523 to 1750 nm using a graded-index multimode optical fiber. *Appl. Phys. Lett.* **102**, 201107 (2013).

14. Fusaro, A. et al. Dramatic acceleration of wave condensation mediated by disorder in multimode fibers. *Phys. Rev. Lett.* **122**, 123902 (2019).
15. Podivilov, E. V. et al. Hydrodynamic 2D turbulence and spatial beam condensation in multimode optical fibers. *Phys. Rev. Lett.* **122**, 103902 (2019).
16. Eftekhari, M. A. et al. Accelerated nonlinear interactions in graded-index multimode fibers. *Nat. Commun.* **10**, 1638 (2019).
17. Lopez-Galmiche, G. et al. Visible supercontinuum generation in a graded index multimode fiber pumped at 1064 nm. *Opt. Lett.* **41**, 2553–2556 (2016).
18. Krupa, K. et al. Spatiotemporal characterization of supercontinuum extending from the visible to the mid-infrared in a multimode graded-index optical fiber. *Opt. Lett.* **41**, 5785–5788 (2016).
19. Agrawal, G. P. *Nonlinear Fiber Optics* 5th edn (Springer, 2000).
20. Zakharov, V. E., L'vov, V. S. & Falkovich, G. *Kolmogorov Spectra of Turbulence I: Wave Turbulence* 1st edn (Springer Science & Business Media, 2012).
21. Picozzi, A. et al. Optical wave turbulence: towards a unified nonequilibrium thermodynamic formulation of statistical nonlinear optics. *Phys. Rep.* **542**, 1–132 (2014).
22. Turitsyna, E. G. et al. The laminar–turbulent transition in a fibre laser. *Nat. Photon.* **7**, 783–786 (2013).
23. Churkin, D. V. et al. Wave kinetics of random fibre lasers. *Nat. Commun.* **6**, 6214 (2015).
24. Sun, C. et al. Observation of the kinetic condensation of classical waves. *Nat. Phys.* **8**, 470–474 (2012).
25. Weill, R., Fischer, B. & Gat, O. Light-mode condensation in actively-mode-locked lasers. *Phys. Rev. Lett.* **104**, 173901 (2010).
26. Wu, F. O., Hassan, A. U. & Christodoulides, D. N. Thermodynamic theory of highly multimoded nonlinear optical systems. *Nat. Photon.* **13**, 776–782 (2019).
27. Makris, K. G., Wu, F. O., Jung, P. S. & Christodoulides, D. N. Statistical mechanics of weakly nonlinear optical multimode gases. *Opt. Lett.* **45**, 1651–1654 (2020).
28. Ramos, A., Fernández-Alcázar, L., Kottos, T. & Shapiro, B. Optical phase transitions in photonic networks: a spin-system formulation. *Phys. Rev. X* **10**, 031024 (2020).
29. Haus, H. A. & Kogelnik, H. Electromagnetic momentum and momentum flow in dielectric waveguides. *J. Opt. Soc. Am.* **66**, 320–327 (1976).
30. Landau, L. D. & Lifshitz, E. M. *Statistical Physics: Volume 5* 3rd edn, Vol. 5 (Butterworth-Heinemann, 1980).
31. Aschieri, P., Garnier, J., Michel, C., Doya, V. & Picozzi, A. Condensation and thermalization of classical optical waves in a waveguide. *Phys. Rev. A* **83**, 033838 (2011).
32. Baudin, K. et al. Classical Rayleigh-Jeans condensation of light waves: observation and thermodynamic characterization. *Phys. Rev. Lett.* **125**, 244101 (2020).
33. Kim, M. Principles and techniques of digital holographic microscopy. *SPIE Rev.* **1**, 018005 (2010).
34. Pathria, R. K. & Beale, P. D. *Statistical Mechanics* (Academic Press, 2011).
35. Siegman, A. *New Developments in Laser Resonators* Vol. 1224 (SPIE, 1990).

Publisher's note Springer Nature remains neutral with regard to jurisdictional claims in published maps and institutional affiliations.

© The Author(s), under exclusive licence to Springer Nature Limited 2022

Methods

Mode-resolved measurements of the electric field. Several techniques for measuring the spatial mode distribution of short light pulses have been reported^{36–39}. However, the measurement of spatiotemporally complex fields is still fairly challenging, especially for fields with a large spacetime-bandwidth product. For the characterization of complex pulsed states, a technique with a readily adjustable spacetime-bandwidth product is desirable. Following an approach developed for the characterization of intense ultrashort pulses at a focus⁴⁰, we employ delay-scanned off-axis digital holography. The pulsed field to be measured is split. One of the copies is spatially filtered to create a Gaussian beam that is used as a spatiotemporal reference beam, and the other (object) is imaged into the camera (Fig. 1b). Fringes caused by the interference of the reference and object fields contain information about the phase of the latter. The electric field $E(x, y, \tau)$ is Fourier transformed to obtain $\tilde{E}(x, y, \omega)$ for the mode decomposition^{41–43}. The spatially filtered reference beam contains all the wavelengths in the original field. At each frequency ω , the complex field $\tilde{E}(x, y, \omega)$ is projected onto the eigenmode basis of the fibre to get the occupancy of the modes. The relative uncertainty in the mode occupancies is estimated to be 10% (Supplementary Section 5). As an example, the frequency-integrated modal decomposition of pulses from one particular state of the mode-locked laser is shown in Supplementary Fig. 5. The beam profile reconstructed from the three-dimensional-field modal decomposition is compared with the measured beam profile to assess the mode decomposition.

In general, results for individual polarizations differ. The modal power fractions $|c_i|^2$ (Fig. 2) include both polarizations. The modal power fraction $|c_{ix}|^2$ and power P_x are measured for one polarization. The process is repeated for the other polarization to yield $|c_{iy}|^2$ and power P_y . The two polarizations are orthogonal; therefore, $|c_i|^2 = (P_x|c_{ix}|^2 + P_y|c_{iy}|^2)/(P_x + P_y)$.

Speckle-pattern generation. To generate the speckle patterns used as the inputs in Fig. 3, we incorporated a reflective phase-only spatial light modulator (SLM; Meadowlark LCoS-1920-1152) in the experimental setup (Fig. 1). The SLM is used in a Fourier-transform configuration, where the Fourier transform of the phase modulation pattern displayed on the liquid crystal screen illuminates the optical fibre. The SLM screen (1,920 pixels \times 1,152 pixels or 17.6 mm \times 10.7 mm) is divided into groups of 128 pixels \times 128 pixels (macro-pixels), resulting in a 15 \times 9 macro-pixel phase array, where each macro-pixel is approximately 1.18 mm \times 1.18 mm, and the phase modulation of each macro-pixel can be arbitrarily chosen between $0 \leq \theta < 2\pi$. By using macro-pixels to create a uniformly distributed random phase array on the SLM, a fully developed speckle pattern illuminates the input facet of the fibre. The SLM is illuminated by the de-chirped pulses from the laser. The laser-illuminated region on the SLM is circular, with a diameter of approximately 9 macro-pixels. A relay lens in a $2f$ configuration (f is the focal length) images the zeroth-order reflection of the SLM phase modulation pattern onto the pupil plane of $\times 10$ objective (LMH-10X-1064), resulting in a circular speckle pattern with an approximate diameter of 20 μ m (approximately nine speckle grains wide). This input illumination pattern is centred relative to the fibre core (Supplementary Section 10).

Numerical simulations. A system of coupled nonlinear Schrödinger equations for the temporal envelopes of the spatial modes is solved. The equations include chromatic and modal dispersions, Kerr and Raman nonlinearities, and self-steepening. The coupled equations are solved with a massively parallel algorithm on a machine with graphical processing unit functionality⁴⁴. This combination reduces the execution time for the relevant simulations of multimode pulse propagation by about two orders of magnitude compared with a standard split-step propagation code run on a central processing unit.

The first 55 transverse spatial modes (first ten mode groups) of the fibre were included in the calculations, which corresponds to propagation constants larger than $\beta = 20 \text{ mm}^{-1}$. Neglecting higher-order modes was necessary to keep the computation times reasonable; even with the parallel code, the execution times exceed several hours for multiple modes with all the relevant short-pulse effects included. We expect the neglect of higher-order modes to be a reasonable approximation given the low observed occupancy of those modes, as well as their uncertainties, in the experiments. In the numerical simulations, 200 fs pulses were launched into 50 cm of the fibre with the experimental parameters. Simulations performed with a variety of different input distributions but the same values of chemical potential and temperature were found to evolve to the same equilibrium state.

Data availability

Source data are available for this paper. Raw data for Figs. 2b, 3e, 4 and 5 are included. All other data that support the plots within this paper and other findings of this study are available from the corresponding author upon reasonable request.

Code availability

The principal components of the codes used in the manuscript have been made publicly available along with extensive documentation at <https://github.com/WiseLabAEP/GMMNLSE-Solver-FINAL>.

References

- Nicholson, J., Yablon, A., Ramachandran, S. & Ghalimi, S. Spatially and spectrally resolved imaging of modal content in large-mode-area fibers. *Opt. Express* **16**, 7233–7243 (2008).
- Rokitski, R. & Fainman, S. Propagation of ultrashort pulses in multimode fiber in space and time. *Opt. Express* **11**, 1497–1502 (2003).
- Guang, Z., Rhodes, M., Davis, M. & Trebino, R. J. Complete characterization of a spatiotemporally complex pulse by an improved single-frame pulse-measurement technique. *J. Opt. Soc. Am. B* **11**, 2736–2743 (2014).
- Guang, Z., Rhodes, M. & Trebino, R. J. Measuring spatiotemporal ultrafast field structures of pulses from multimode optical fibers. *Appl. Opt.* **56**, 3319–3324 (2017).
- Pariante, G., Gallet, V., Borot, A., Gobert, O. & Quéré, F. Space-time characterization of ultra-intense femtosecond laser beams. *Nat. Photon.* **10**, 547–553 (2016).
- Shapira, O., Abouraddy, A. F., Joannopoulos, J. D. & Fink, Y. Complete modal decomposition for optical waveguides. *Phys. Rev. Lett.* **94**, 143902 (2005).
- Lü, H., Zhou, P., Wang, X. & Jiang, J. Fast and accurate modal decomposition of multimode fiber based on stochastic parallel gradient descent algorithm. *Appl. Opt.* **52**, 2905–2908 (2013).
- Paurisse, M., Lévêque, L., Hanna, M., Druon, F. & Georges, P. Complete measurement of fiber modal content by wavefront analysis. *Opt. Express* **20**, 4074–4084 (2012).
- Wright, L. G. et al. Multimode nonlinear fiber optics: massively parallel numerical solver, tutorial and outlook. *IEEE J. Sel. Topics Quantum Electron.* **24**, 1–16 (2018).

Acknowledgements

This effort was sponsored, in part, by the Department of the Navy, Office of Naval Research, under award nos. N00014-20-1-2789 (P.S., N.B., F.W., F.O.W. and D.N.C.) and N00014-18-1-2347 (D.N.C.). Portions of the work were sponsored by the National Science Foundation award nos. ECCS-1912742 (H.P. and F.W.) and EECS-1711230 (F.O.W. and D.N.C.), the Army Research Office (award no. W911NF1710481 (D.N.C.)), the Simons Foundation (733682 (D.N.C.)) and the BSF (2016381 (D.N.C.)).

Author contributions

H.P., P.S. and N.B. conducted the experiments and performed the data analysis. L.W. developed the laser and P.S. developed the spatiotemporal measurement instrument. H.P. and F.O.W. performed the numerical simulations. F.O.W. and D.N.C. developed the theory. L.W., H.P., F.O.W., N.B. and F.W. conceived the experiments. All the authors contributed to the writing and editing of the manuscript.

Competing interests

The authors declare no competing interests.

Additional information

Supplementary information The online version contains supplementary material available at <https://doi.org/10.1038/s41567-022-01579-y>.

Correspondence and requests for materials should be addressed to Frank Wise.

Peer review information *Nature Physics* thanks the anonymous reviewers for their contribution to the peer review of this work.

Reprints and permissions information is available at www.nature.com/reprints.